DIRECT SIMULATIONS OF THERMOACOUSTIC HEAT EXCHANGERS

O. M. Knio[†], E. Besnoin

Department of Mechanical Engineering, The Johns Hopkins University, USA

[†]Email: knio@jhu.edu

Abstract

The performance of an idealized thermoacoustic refrigerator is analyzed using direct numerical simulations. The model is based on a combination of quasi-1D resonant tube acoustics with multi-dimensional transient simulations of the flow and temperature fields in the neighborhood of the thermoacoustic stack and heat exchangers. The latter are described using a vorticity-based model that simulates the compressible conservation equations in the low-Mach-number limit. Model predictions are validated by comparing computed results with corresponding PIV measurements of the velocity and vorticity distributions around the plate edges. Computations are then applied to analyze the effects of heat exchanger length and position on the performance of the device and on the flow behavior. The results indicate that the cooling load peaks at a well-defined combination of heat exchanger length and gap width between the heat exchangers and the stack plates. At high drive ratio, the flow exhibits sustained unsteady behavior and is characterized by the appearance of a large-amplitude wavy motion within the gap, between the plates and in the vicinity of the thermoacoustic stack. It is also found that this phenomenon leads to enhancement of the cooling load and affects optimal heat exchanger parameters.

Introduction

As schematically illustrated in figure 1, a thermoacoustic refrigerator typically comprises a resonance tube that houses a stack of parallel plates, an acoustic source, and heat exchangers. The operating principle of the device is the well-known thermoacoustic effect [1], [2], which results in transport of heat from one end of the stack to the other. By placing hot and cold heat exchangers close to the ends of the stack plates, the thermo-acoustically generated heat flux can be exploited to drive a refrigeration cycle. The mechanics of the mean energy transport between the stack plates is relatively well understood, and is in most cases adequately described using the well-known linearized theory [2]. In contrast, the behavior of thermoacoustic heat exchangers is far more challenging, in large part due to presence of concentrated eddy structures in the neighborhood of plate ends [3], [4], [5], [6], [7], [8], [9], [10]. Consequently, effective design and optimization of thermoacoustic refrigerators necessitates a fundamental understanding of these vortical motions, and

their dependence on geometric parameters and operating conditions.
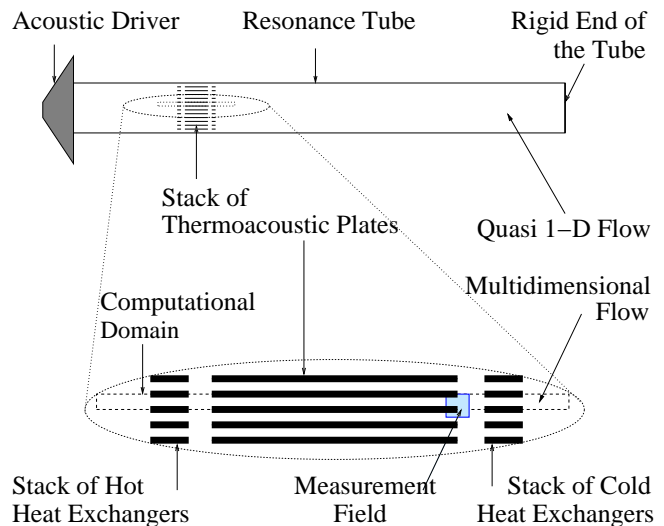

Figure 1: Schematic illustration of the thermoacoustic refrigerator (top) with a magnified view of the computational domain (bottom)

This paper discusses recent results of a computational effort [7], [10], [11] that aims at investigating the flow features around, and heat transfer behavior of thermoacoustic heat exchangers. The model is based on a simplified representation of resonance tube acoustics and on detailed (2D) representation of the unsteady flow in a neighborhood of the stack and heat exchangers. Earlier versions of the numerical model [4], [8] were validated after comparison with linear theory predictions, experimental data for a thermoacoustic couple [12] and numerical results obtained using a finite-volume model [8]. Recent improvements account for finite plate thickness, where the stack and heat exchangers plates are no longer treated as vanishingly thin, and the effect of a gap between the stack and heat exchanger plates. Numericaly obtained visualizations of the unsteady flow field around the edges of a thermoacoustic stack are first compared with time-resolved PIV measurements [7] of the velocity and vorticity fields [9] obtained at similar conditions. We focus on stacks operating at low drive ratios, and present results obtained with two stack configurations that are characterized by disparate ratios of the plate thickness to the viscous penetration depth. This enables us to contrast experimental and computational predictions in distinct flow regimes. The simulations are then used to analyze the combined

effects of geometrical parameters and operating conditions on the behavior of the cooling load and on the basic features of the flow.

Numerical Model

The simulations of the unsteady flow are performed using a computational model that is an extended version of the scheme originally introduced in [3]. The model relies on a simplified representation of the effect of the resonant standing wave, and on a fully-resolved representation of the flow in the neighborhood of the stack and heat exchangers. The physical formulation is based on the vorticity-form of the compressible conservation equations in the low-Mach-number limit. A second-order finite-difference discretization of the equations of motion is used in conjunction with explicit third-order time integration of the discretized evolution equations. The discrete system also includes elliptic equations for the streamfunction and velocity potential, which are efficiently inverted using a specially-tailored domain decomposition approach. This approach enables us to split the original systems into elliptic systems in rectangular subdomains. These subsystems are efficiently inverted using FFT-based Poisson solvers and the overall solution is reconstructed using an influence matrix method. Additional details on the numerical scheme can be found in [7], [11].

Flow Visualization

Numericaly obtained visualizations of the unsteady flow field around the edges of a thermoacoustic stack are compared with time-resolved PIV measurements [7] of the velocity and vorticity fields [9] around the stack plates and in the absence of heat exchangers. As summarized in Table 1, two stack configurations are considered in the experiments. In both cases, the center of the stack is located midway between the velocity node and the velocity anti-node, i.e. at a non-dimensional wave-number $kx = 3\pi/4$. In addition to the ge-

Table 1: Geometric and flow parameters for configurations A and B. d and L_p are the thickness and length of the stack plates, respectively, h is the distance between two consecutive plates.

	Configuration A	Configuration B
d (mm)	1.0	0.15
h (mm)	2.0	1.0
L_p (mm)	25.8	24.0
Dr (%)	0.5	1.5
h/δ_ν	13.	6.7
d/δ_ν	6.5	1.0

ometrical parameters of the stack, the computations use as input the thermal properties of the stack plates and of air, as well as the mean pressure and temperature, respectively $P_m = 10^5$ N/m^2 and $T_m = 300°$K. The experimentally-observed frequency of the resonant standing wave, $f = 200$ Hz is also used as input. Meanwhile, the amplitude of the standing wave is expressed in terms of the drive ratio, Dr, which expresses the ratio of the acoustic pressure amplitude to the mean pressure (Table 1). As can be appreciated from Table 1, the two stack configurations are geometrically similar, and are nearly equal in length. However, the thickness and spacing of the stack plates are significantly smaller in configuration A than they are in configuration B. These differences are also highlighted by providing the ratios h/δ_v and d/δ_v, where δ_v is the viscous penetration depth [2]. Thus, d is substantially larger than δ_v in configuration A, but is close to δ_v in configuration B. Accordingly, we shall refer to these two stacks as thick-plate and thin-plate configurations, respectively.

In both the experiments and computations, data analysis is performed when a "periodically-steady" state is established. This occurs after a large number of acoustic cycles, during which the initial starting transient decays. Once steady state is achieved, instantaneous data on the velocity and vorticity fields is collected at well defined instants within a single cycle. In both the experiments and computations, 16 equally-spaced, instantaneous realizations are obtained, starting at $t = t_p$, which is the time at which the (imposed) acoustic pressure signal peaks within the acoustic cycle.

Thick-plate configuration

Figure 2 depicts an instantaneous realization of the velocity and vorticity fields for configuration A. Results shown on top are obtained experimentally [9]; the corresponding computational predictions shown at the bottom are obtained at $t_p + 3T/16$. Note that the frame of the computational results has also been restricted to match the 4.2×4.2 mm^2 window of the PIV measurements. As schematically illustrated in Fig. 1, this "test section" is located near the cold-end of the stack plates. In particular, the results are arranged in such a way that the velocity node is located to the left of each frame.

For the present configuration, both the experimental and computational results reveal the presence of concentrated vortices near the edge of the plate. Also evident is the presence of both signs of vorticity, both inside the channel and in the open region. The generation of alternating layers of vorticity within the channel is not surprising, since the ratio of channel height to viscous penetration depth is large and the development of Stokes layers within the channel is accordingly expected. As can be observed in Fig. 2, the vorticity dis-

tribution outside the channel can also exhibit complex structure, especially when separated vortices are driven back into the channel and impinge on the edge of the plates.
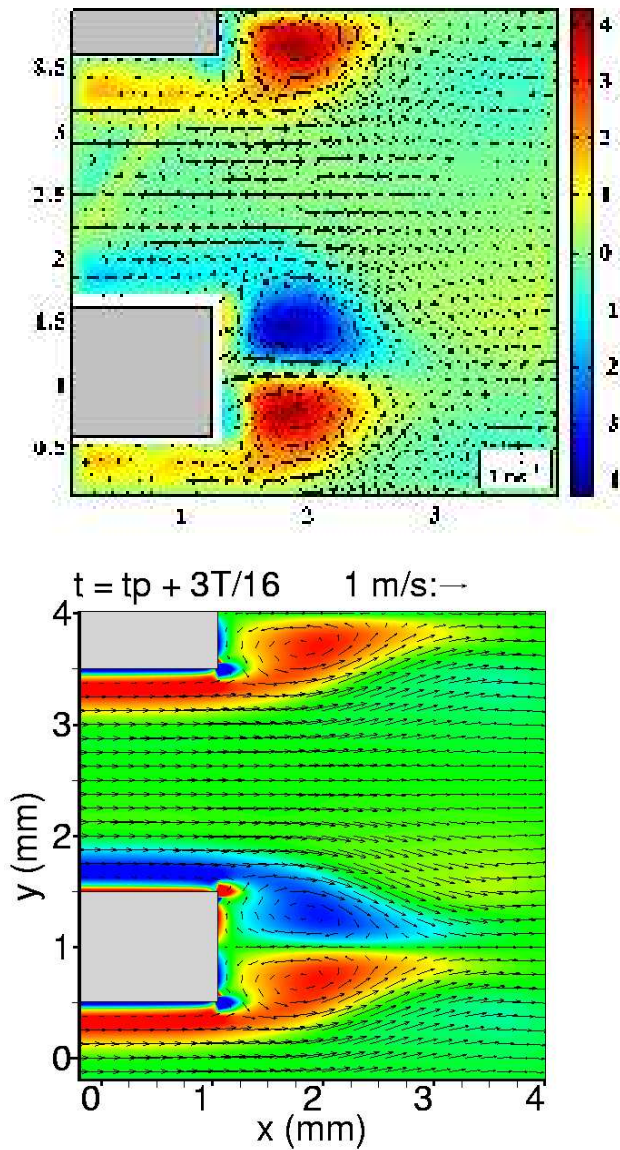

Figure 2: Velocity vectors and vorticity fields in the fluid around the edges of the stack plates obtained experimentally (top) and numerically (bottom) with configuration A in Table 1.

Comparison of the experimental and computational results in Fig. 2 reveals a close correspondence between the predictions. In particular, at both phases, very good agreement can be observed between peak vorticity values as well as the size of the recirculating regions.

Thin-plate configuration

Figure 3 provides computed and experimental results obtained for configuration B. Computed velocity and vorticity distribution are shown at the bottom and con-

tours of the experimental vorticity distribution at the corresponding times are shown on top. The figure is generated in a similar fashion as in Fig. 2, i.e. the computational test section is restricted so that it matches the experimental window. In the present case, the PIV measurements are performed in a 2.9×2.3 mm^2 window, also located near the cold end of the stack.

The present predictions are thus in sharp contrast with earlier observations. Specifically, in the present case the results do not show the formation of well-defined eddies. The vorticity distribution in the wake exhibits the presence of elongated layers that extend well outside the channel. However, significant rollup of these layers is not observed, although evidence of very weak recirculating motion near the plate corners can be detected in the computational frame.
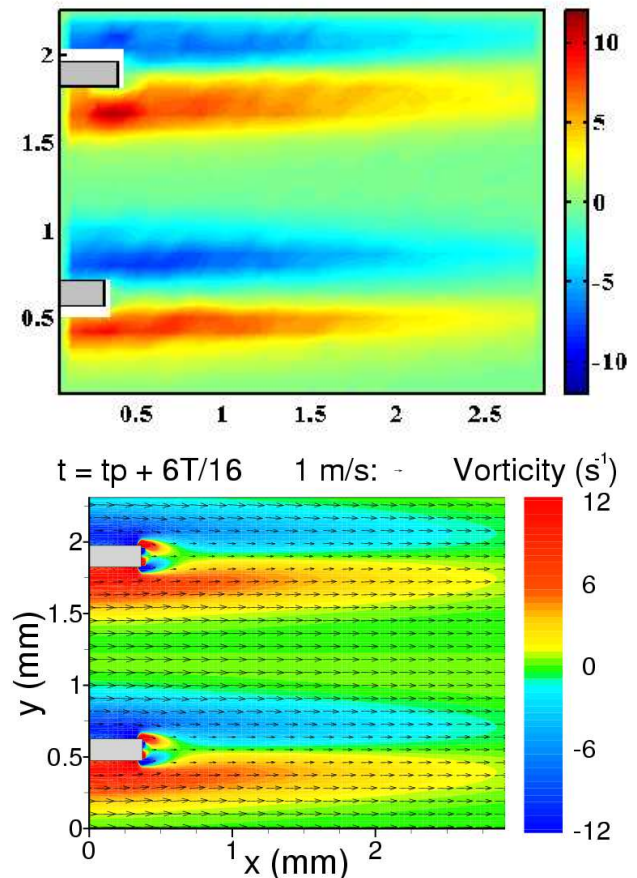

Figure 3: Vorticity fields (top) in the fluid around the edges of the stack plates obtained experimentally with configuration B. The numerical prediction in the same configuration for the velocity vectors and vorticity fields are shown at the bottom.

Parametric Study

The numerical model is applied to study the effect of geometrical parameters and operating conditions on the performance of the device and on the flow dynam-

ics. In all the cases considered, the center of the stack is located midway between the velocity node and the velocity antinode, i.e. at a non-dimensional wavenumber $kx = 3\pi/4$. The stack plates are 3.18-cm long with a thermal conductivity $\tilde{k}_s = 0.482$ W/m·°K. We assume that the resonance tube is filled with Helium with mean temperature $\tilde{T}_m = 300°$K and mean pressure $\tilde{P}_m = 10^5$ N/m^2. The frequency of the standing wave $\tilde{f} = 707$ Hz and the acoustic wavelength $\tilde{\lambda} = 1.44$ m. A parametric study is performed of the effects of gap width ($\tilde{g}$) between the heat exchangers and the stack plates, heat exchanger length ($\tilde{L}_c$). The analysis is conducted for different drive ratio ($2\% \leq$ Dr $\leq 8\%$), temperature difference between the hot and cold heat exchangers ($6\,K \leq \Delta\tilde{T} \leq 21\,K$). We start by analyzing the behavior of the cooling load ($\tilde{Q}_{m,f\rightarrow c}$) and then examine the flow structure for selected configurations and operating conditions.

Cooling load

As shown in Fig 4, the cooling load ($\tilde{Q}_{m,f\rightarrow c}$) peaks at a well-defined combination of the gap width and heat exchanger length, which varies with the drive ratio, and temperature difference between the heat exchangers. For the present conditions, $(L_c, g)_{opt} \simeq (1.5, 0.4)$. For larger and smaller gaps the cooling load drops rapidly, with variations of up to 100% in the range considered. Note that the decrease in the cooling load at large values of $\tilde{g}$ is expected. This is the case because the exchange between the stack and the heat exchangers is governed by particle transport and is consequently limited by the particle displacement amplitude. Thus, as the gap becomes large, the thermal coupling between the stack and heat exchangers is diminished, and the cooling load is consequently reduced. The reverse effect, namely the drop in the mean heat flux as $\tilde{g}$ becomes small, results from the increase in reverse heat transfer as $\tilde{g}$ decreases.

Further analysis of the results leads to the identification of two parameters, namely the optimal heat exchanger length (L_{opt}) and the optimal gap width (g_{opt}). L_{opt} denotes the ratio of the heat exchanger length ($\tilde{L}_{h/c}$) to ($2\tilde{R}_p + \tilde{\delta}_k$) for which the cooling ($\tilde{Q}_{m,f\rightarrow c}$) peaks when the gap width (g) is kept constant. On the other hand, g_{opt} denotes the ratio of the gap width (g) to ($2R_p + \delta_k$) for which the cooling peaks when the heat exchanger length ($L_{h/c}$) is kept constant. As illustrated in Fig 5, it appears that the optimal length varies only with the gap width and with the plate separation distance; it does not depend on any of the other parameters studied here. On the other hand and as also shown in Fig 5, the optimal gap width is independent of the heat exchanger length, so long as $L_c/L_o > 1$. The optimal gap becomes wider when the temperature difference between the heat exchangers is increased.
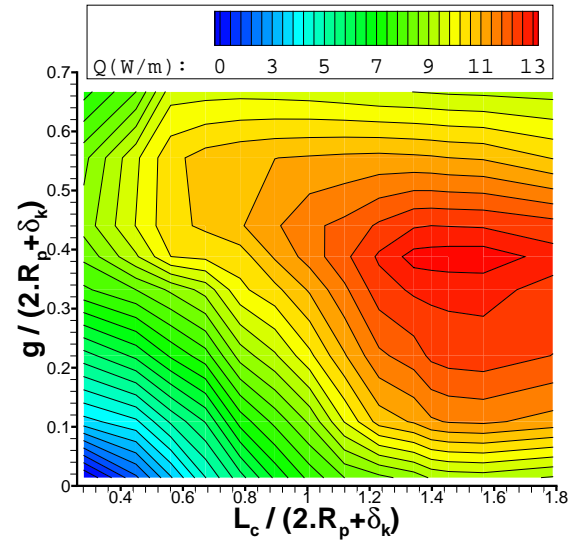

Figure 4: Contours of $\tilde{Q}_{m,f\rightarrow c}$ for different values of L_c and g. Curves are obtained with $\Delta\tilde{T} = 18$ K and $Dr = 8\%$.

Note also that depending on the configurations considered, the normalized heat exchanger length for which the cooling load peaks varies between $L_{c/h}/(2R_p + \delta_k) \simeq 0.7$ and $L_{c/h}/(2R_p + \delta_k) \simeq 1.9$ (not shown). This result strongly contrasts with results obtained in the thin-plate limit [8], where the cooling was found to peak when $L_{c/h}/(2R_p + \delta_k) \simeq 0.3$ and with Swift's analysis [2], which predicts peak performance when the length of the cold heat exchangers is approximately equal to $(2R_P + \delta_k)$.

Flow structure

The analysis of the effect of the drive ratio (Dr) and gap width (g) on the structure of the flow near the heat exchangers reveals three distinct flow regimes, namely low, moderate and high drive ratio regimes. For all the cases considered, with $Dr \leq 3\%$ the flow field remains symmetric throughout the acoustic cycle. Breaking of the flow symmetry first occurs at moderate drive ratio - $3.5 \leq Dr \leq 5\%$ - when the gap between the stack and heat exchangers is sufficiently wide. In this regime, breaking of the symmetry occurs during the deceleration phase, during which the particles heat up. A wave-like pattern grows and a sequence of vortices appears downstream, which entrain warm fluid toward the edge of the cold heat exchanger, as shown in Fig. 6. In the present case, the presence of a wide gap between heat exchangers and stack plates prevents these vortices from reaching the cold heat exchanger and penetrating the thermal boundary layer. As a result, reverse heat transfer is minimized. This configuration is however not optimal. As shown in Fig. 5, the overall cooling load peaks when the gap is narrower, at
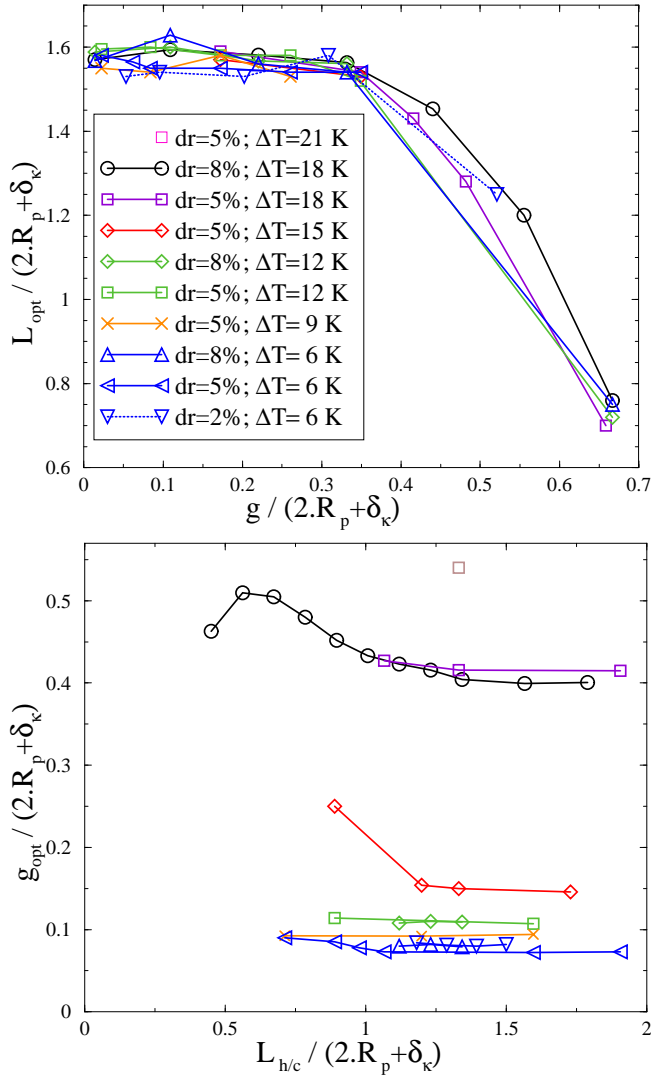
Figure 5: Variation of the optimal heat exchanger length with gap width (top) and of the optimal gap width with heat exchanger length (bottom). L_{opt} is defined as the heat exchanger length for which the flux peaks for a given (fixed) gap width; g_{opt} is defined as the gap with between heat exchangers and stack plates for which the flux peaks for a given (fixed) heat exchanger length.

Figure 6: Temperature distribution and velocity vectors around the thermoacoustic stack (top) and the cold heat exchanger (bottom) for $Dr = 5\%$, $\Delta \tilde{T} = 18$ K, $L_{c/h}/Lo = 1.33$, and $g/L_o = 0.659$.

$g/(2.R_p + \delta_k) \simeq 0.4$. This is the case because the thermal coupling between plates and heat exchangers is diminished as the gap is widened. This is followed by a second deceleration phase, during which the particles cool down. The sequence of events described above is repeated in the opposite direction, and cold core vortices are convected towards the edges of the stack plate in a similar fashion as that illustrated in Fig. 6, contributing to the thermal coupling between stack and cold heat exchanger [7], [11]. Note also that an analysis of the flow patterns around the other edge of the cold heat exchanger reveals that the flow is symmetric throughout the acoustic cycle in this particular configuration.
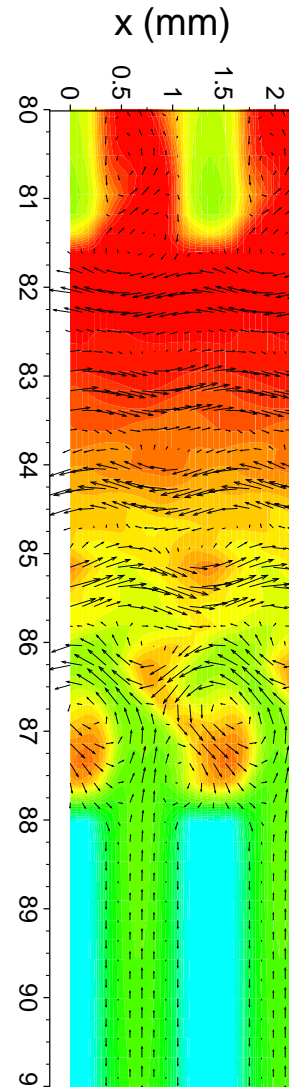
Qualitatively, the flow patterns in this region are similar to those around the edges of isolated stack plates, as discussed earlier. At high drive ratio - when $Dr \geq 6.5\%$ - asymmetric flow patterns and heat transfer rates occur which are similar to those described at moderate drive ratio with wide gap. However, in the high drive ratio regime, these asymmetric patterns are observed for all values of the gap width and of the temperature difference between cold and hot heat exchangers. In addition, the analysis reveals that when $Dr \geq 6.5\%$, this phenomenon is accompanied by the appearance of a large-amplitude wavy motion within the gap and between the plates, as well as outside the thermoacoustic stack, as shown in Fig. 7. The vortices appear stronger as the drive ratio increases, and their impingement on solid surfaces results in inhomogeneous heat flux. Because
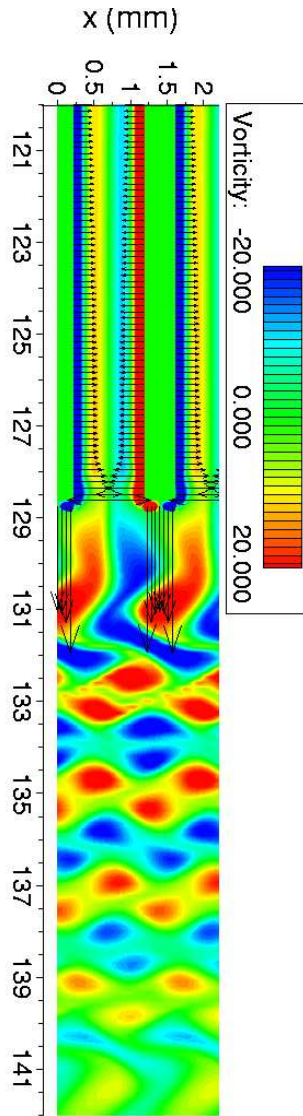
Figure 7: Vorticity distribution around and heat flux vectors along the surface of the cold heat exchanger. The plots are generated for $Dr = 8\%$, $\Delta\tilde{T} = 18$ K, $L_{c/h}/Lo = 1.23$, and $g/L_o = 0.33$, with $L_o = (2.R_p + \delta_k)$.

of the increased transport of low-temperature core flow along the plate by the vortices, the warmer particles are carried away from the cold heat exchangers more efficiently. As a result, the gap required to attenuate the detrimental effect of reverse heat transfer through the edges of the heat exchanger is smaller than that required at low drive ratios, where the flow patterns remain symmetric, which explains the trends shown in Fig. 5.

References

[1] Lord Rayleigh, Theory of Sound, 1945.

[2] G.W. Swift, "Thermoacoustic Engines," J. Acoust. Soc. Am., 84:1145-1180, 1988.

[3] A.S. Worlikar, O.M. Knio, and R. Klein, "Numer-

ical simulation of thermoacoustic refrigerator Part II: Stratified flow around the stack," J. Comput. Phys., 144:299–324, 1998.

[4] A.S. Worlikar and O.M. Knio, "Numerical Study of Oscillatory Flow and Heat Transfer in a Loaded Thermoacoustic Stack," Numerical Heat Transfer A, 35:49-65, 1999.

[5] M. Wetzel and C. Herman, "Experimental study of thermoacoustic effects on a single plate Part I: Temperature fields," Heat and Mass Transfer, 36:7-20, 2000.

[6] M. Wetzel and C. Herman, "Experimental study of thermoacoustic effects on a single plate Part II: Heat transfer," Heat and Mass Transfer, 35:433-441,1999.

[7] E. Besnoin, Computational Study of Thermoacoustic Heat Exchangers, Ph.D. Thesis, The Johns Hopkins University, Baltimore, Maryland, 2001.

[8] E. Besnoin and O.M. Knio, "Numerical study of thermoacoustic heat exchangers in the thin-plate limit," Numerical Heat Transfer A, 40:445-471, 2001.

[9] S. Duffourd, Refrigerateur thermoacoustique: études analytiques et experimentales en vue d'une miniaturisation, Ph.D. Thesis, Ecole Centrale de Lyon, 2001.

[10] Blanc-Benon P., Besnoin E., Knio O., "Experimental and computational visualization of the flow field in a thermoacoustic stack, Compte Rendus de l'Académie des sciences, 331:17-24, 2003.

[11] E. Besnoin and O.M. Knio, "Numerical Study of Thermoacoustic Heat exchangers," to appear in Acustica.

[12] A.A. Atchley, T.J. Hofler, M.L. Muzzerall, M.D. Kite, and C. Ao, "Acoustically generated temperature gradients in short plates," J. Acoust. Soc. Am., 88:251-263, 1990.